NANO LETTERS

pubs.acs.org/NanoLett Letter

Origin of Superionic $Li_3Y_{1-x}In_xCl_6$ Halide Solid Electrolytes with High Humidity Tolerance

Xiaona Li,[#] Jianwen Liang,[#] Keegan R. Adair,[#] Junjie Li, Weihan Li, Feipeng Zhao, Yongfeng Hu, Tsun-Kong Sham, Li Zhang, Shangqian Zhao, Shigang Lu, Huan Huang, Ruying Li, Ning Chen,* and Xueliang Sun*

Cite This: *Nano Lett.* 2020, 20, 4384−4392 Read Online

ACCESS | Metrics & More | Article Recommendations | Supporting Information

ABSTRACT: The high ionic conductivity, air/humidity tolerance, and related chemistry of Li_3MX_6 solid-state electrolytes (SSEs, M is a metal element, and X is a halogen) has recently gained significant interest. However, most of the halide SSEs suffer from irreversible chemical degradation when exposed to a humid atmosphere, which originates from hydrolysis. Herein, the function of the M atom in Li_3MX_6 was clarified by a series of $Li_3Y_{1-x}In_xCl_6$ ($0 \le x < 1$). When the ratio of In^{3+} was increased, a gradual structural conversion from the hexagonal-closed-packed (hcp) anion arrangement to cubic-closed-packed (ccp) anion arrangement has been traced. Compared to hcp anion sublattice, the Li_3MX_6 with ccp anion sublattice reveals faster Li^+ migration. The tolerance of $Li_3Y_{1-x}In_xCl_6$ towards humidity is highly improved when the In^{3+} content is high enough due to the formation of hydrated intermediates. The correlations among composition, structure, Li^+ migration, and humidity stability presented in this work provide insights for designing new halide-based SSEs.

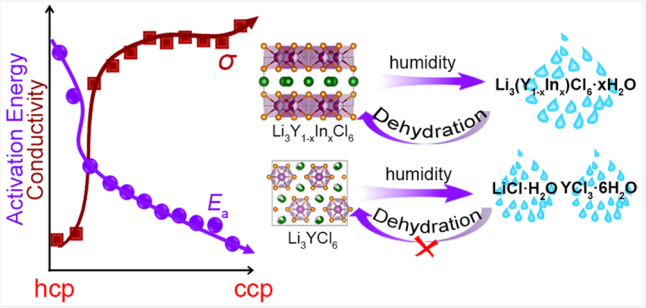

KEYWORDS: *halide solid electrolyte, humidity, all-solid-state, anion sublattice, lithium-ion conductor*

Solid-state electrolytes (SSEs) are key materials for the development of next-generation of all-solid-state lithium batteries (ASSLBs).[1,2] Several different types of SSEs have been developed including polymer-, oxide-, sulfide-, borohydride-, and halide-based SSEs.[2,3] An anionic halide compound that is more electronegative than the alternative oxide and sulfide, etc. can achieve thermodynamically electrochemical stability windows higher than 4 V (chloride) and 6 V (fluoride).[4,5] Furthermore, the combination of several positive attributes, such as the high room-temperature (RT) ionic conductivities,[6−10] the good stability toward oxide cathode,[4] and even the water-based synthesis routes,[8] has made the halide SSEs quite attractive.

Early halide SSEs[11−13] played a crucial role in understanding the Li^+ diffusion in SSEs. Based on this, some high ionic conductivity materials such as Li_3MX_6 (M is a metal element, and X is a halogen) have been proposed.[6−9,14,15] Although the crucial role of phase structure and site occupation on the effect of ionic conductivity was highlighted by detailed investigations on these types of SSEs, much remains to be understood for further fundamental insights that will ultimately lead to implementable solutions. Furthermore, scientists found that in the Li_3InCl_6 SSEs, both high ionic conductivity and humidity/air tolerance are possible.[7,8] However, until now, most halide SSEs have shown no tolerance to humidity. The chemical degradation and the related mechanism remains unclear. Thus, deciphering the degradation/tolerance process in such halide SSEs could be of significant importance.

Here, we demonstrate the feasibility of increasing the humidity tolerance and the ionic conductivity in $Li_3Y_{1-x}In_xCl_6$ ($0 \le x < 1$) by optimizing the metal central atom based on the different coordination chemistry of In^{3+}/Y^{3+}. The changes in the crystal structure and humidity stability have been monitored by X-ray diffraction (XRD), X-ray absorption near edge structure (XANES), and extended X-ray absorption fine structure (EXAFS) analysis. The results show that the pristine hexagonal-closed-packed (hcp) anion sublattice structure of Li_3YCl_6 gradually changes to the cubic-closed-packed (ccp) anion sublattice structure with increasing In^{3+} content, and the highest ionic conductivity is achieved with 50% In^{3+} substitution. The humidity tolerance of $Li_3Y_{1-x}In_xCl_6$ SSEs is improved by increasing the amount of In^{3+} since more In^{3+} aids

Received: March 16, 2020
Revised: May 4, 2020
Published: May 14, 2020

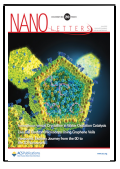

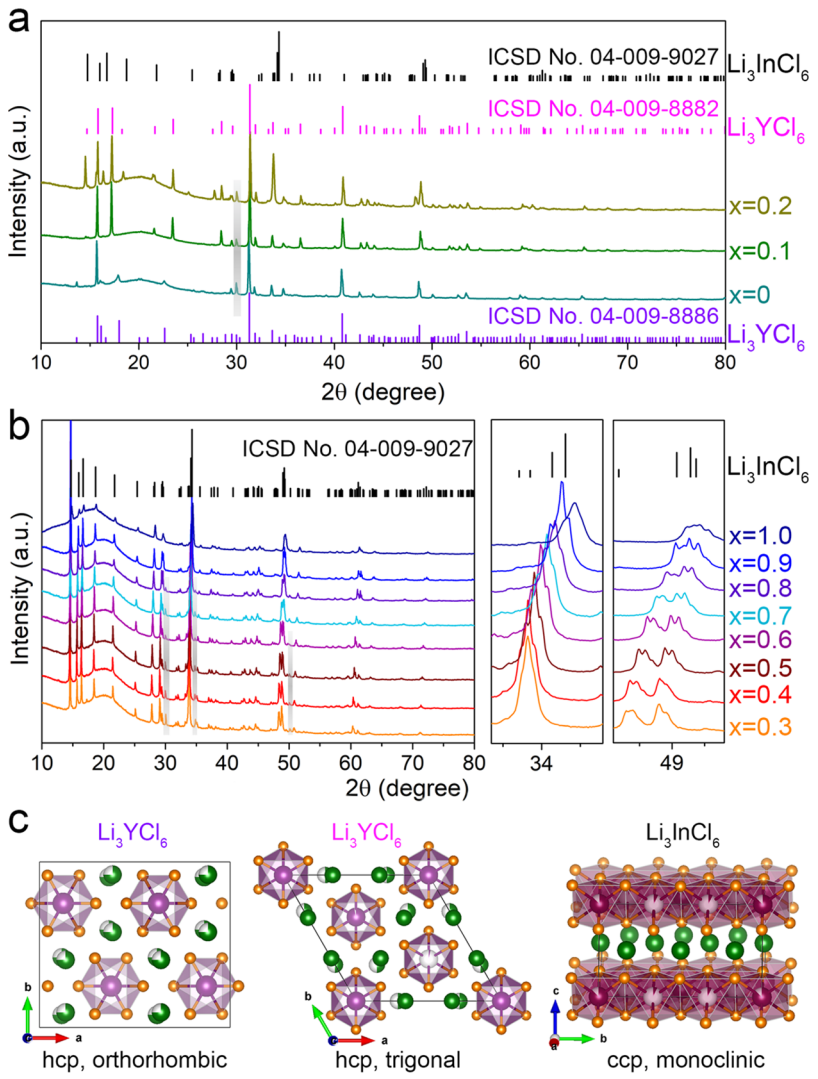

Figure 1. (a) XRD patterns of $Li_3Y_{1-x}In_xCl_6$ (x = 0, 0.1, 0.2). (b) XRD patterns of $Li_3Y_{1-x}In_xCl_6$ (x = 0.3−1.0). The gray bars indicate the reflections of LiCl. (c) Structures of Li_3YCl_6 and Li_3InCl_6 based on the database.

in the formation of hydrated intermediates rather than separated phases. Ultimately, the work presented herein improves our understanding of the structural properties and the humidity tolerance in halide SSEs, thereby providing insights for the development of future electrolytes.

Results and Discussion. $Li_3Y_{1-x}In_xCl_6$ ($0 \le x \le 1$) was prepared from LiCl, YCl_3, and $InCl_3$ at 260 °C after ball milling. Without In^{3+} substitution (x = 0), the XRD pattern can be indexed to orthorhombic Li_3YCl_6 (ICSD No. 04-009-8886),[16] while the XRD pattern changed to the trigonal Li_3YCl_6 structure (ICSD no. 04-009-8882)[16] when x = 0.1 (Figure 1a). When x = 0.2, the main phase is still trigonal Li_3YCl_6 and some new peaks of the monoclinic Li_3InCl_6 structure ($C2/m$, ICSD no. 04-009-9027)[17] appeared (Figure 1a). The obvious monoclinic Li_3InCl_6 phase starts to evolve at $x \ge 0.3$, with all of the XRD patterns being quite similar (Figure 1b). Figure 1c shows the crystal structures of orthorhombic/trigonal Li_3YCl_6 and monoclinic Li_3InCl_6. The anion arrangement of the orthorhombic Li_3YCl_6 (Table S1) can be regarded as an hcp structure.[18] All the cations occupy the octahedral sites formed by Cl^- anions. The trigonal Li_3YCl_6 structure (Table S2) is also based on an hcp anion arrangement with different Y^{3+} and Li^+ sites,[16] while the monoclinic Li_3InCl_6 structure (Table S3) is based on a ccp anion arrangement.

Rietveld XRD Refinement was performed to obtain the detailed lattice parameter evolutions of $Li_3Y_{1-x}In_xCl_6$ ($0.3 \le x \le 0.9$, Figure S1 and Table S4). As a result, the Y atoms are occupied in the 4g position together with In, leaving the other 2a position vacant. With the decreasing Y^{3+} content, all lattice parameters of a, b, and c decrease, and the values for parameters of a and b begin to converge (Figure S2a). Thus, the decreasing of Y^{3+} content leads to a shrinkage of the $(Y/In)Cl_6^{3-}$, $LiCl_6^{5-}$ octahedra, and the unit cell volume (Figure S2b−d). Such shrinkage of the lattice parameters should be due to the smaller In^{3+} (80 pm) than Y^{3+} (90 pm).[19]

DFT calculations were conducted to assess the thermodynamically favourable Y locations (Y_{In}) in $Li_3Y_{1-x}In_xCl_6$ ($x \ge 0.3$). Since there are two In positions in monoclinic Li_3InCl_6, three structures were considered in the DFT calculations: (1) pristine Li_3InCl_6; (2) Y in the 4g (In_1) position; (3) Y in the 2a (In_2) position. The Y_{In} formation energies of the three structures were compared in Figure S2e. The Y in the In_1 site leads to the lowest formation energy among the three structures, indicating the preferred Y location in the In_1 site to form $(Y/In)Cl_6^{3-}$ octahedra within the structure. Moreover,

https://dx.doi.org/10.1021/acs.nanolett.0c01156
Nano Lett. 2020, 20, 4384−4392

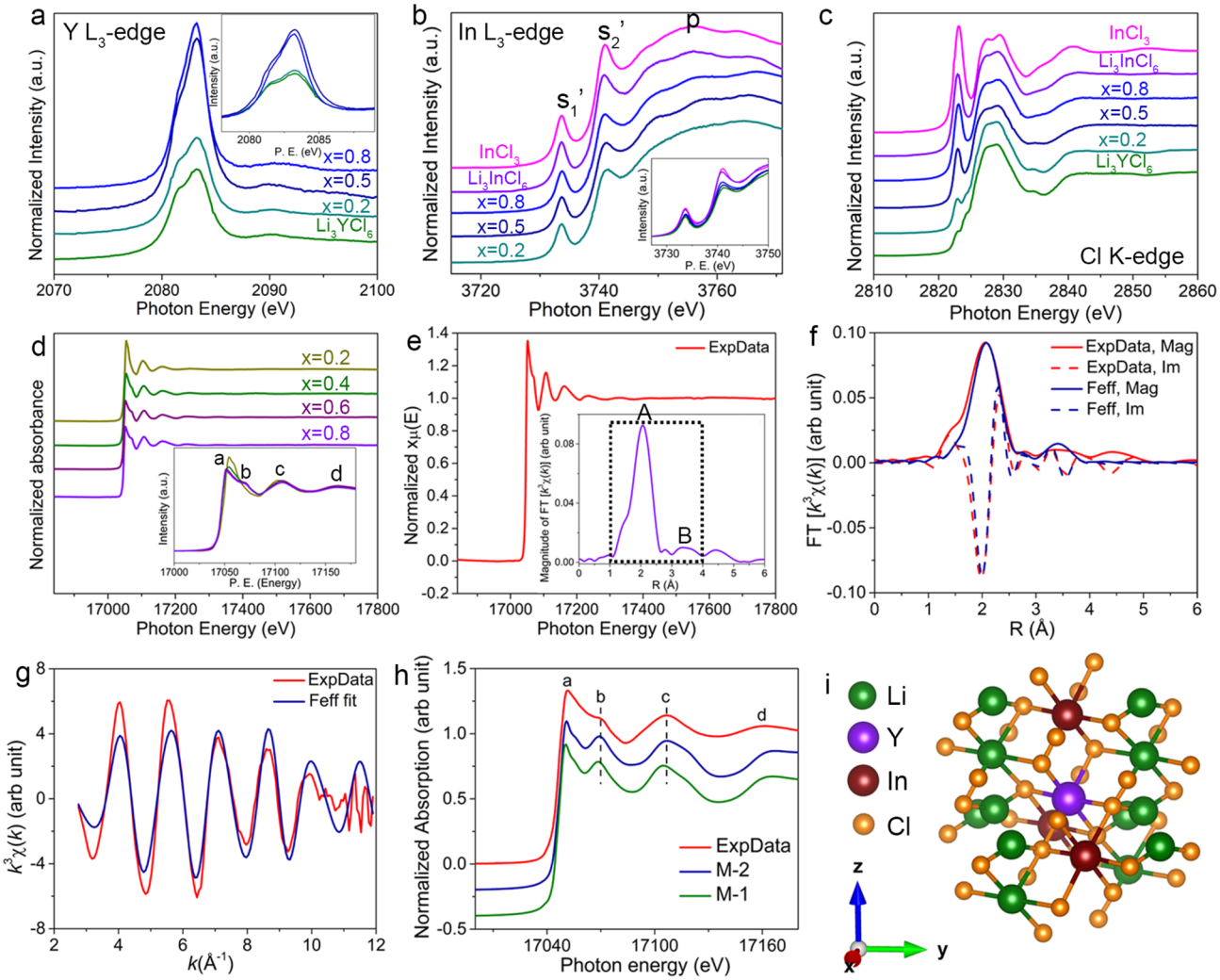

Figure 2. Normalized (a) Y L_3-edge XANES spectra of $Li_3Y_{1-x}In_xCl_6$ SSEs (x = 0, 0.2, 0.5, 0.8), (b) In L_3-edge XANES spectra of commercial $InCl_3$ and $Li_3Y_{1-x}In_xCl_6$ SSEs (x = 0.2, 0.5, 0.8, 1), and (c) Cl K-edge XANES spectra of commercial $InCl_3$, and $Li_3Y_{1-x}In_xCl_6$ SSEs (x = 0, 0.2, 0.5, 0.8, 1). Normalized (d) Y K-edge XAFS spectra of $Li_3Y_{1-x}In_xCl_6$ SSEs (x = 0.2, 0.4, 0.6, 0.8); (e) Y K-edge XAFS spectroscopy of $Li_3Y_{0.2}In_{0.8}Cl_6$. The inset figure is the magnitude of FT for $k^3\chi(k)$ of the experimental data and experimentally resolved EXAFS features "A" and "B". (f) The magnitude and imaginary part of FT between the experimental (red solid and red dash traces) and the Feff modeling (blue solid and blue dash traces) of Y_{In} in 4g in $Li_3Y_{0.2}In_{0.8}Cl_6$; (g) $k^3\chi(k)$ between the experimental and the R space curve fitting guided Feff modeling of Y_{In} in 4g in $Li_3Y_{0.2}In_{0.8}Cl_6$ based on the R space curve fitting result. (h) Comparison between the experimental XANES (red line) and the XANES theoretical modeling (green for M-1 modeling and blue for M-2 modeling). (i) The XAFS model M-2 structural system based on the crystallography of $Li_3Y_{0.2}In_{0.8}Cl_6$ (Y centered spherical clusters with a radius of 6.0 Å).

the reduced formation energies compared to the pristine Li_3InCl_6 demonstrates the favorable Y^{3+} incorporation into the structure.

The structures of $Li_3Y_{1-x}In_xCl_6$ SSEs were further investigated by XANES. The Y L_3-edges in Figure 2a show mostly a split double-peak, with varied intensity ratios and separations between the two peaks located at 2081.7 and 2083.2 eV, which are consistent with the previous report of Y^{3+} species with six-coordinated Y atoms.[20,21] There's no obvious difference in the Y L_3-edge XANES spectra of Li_3YCl_6 and x = 0.2, while a sudden change occurred at x = 0.5 with no further changes afterward, which should be related to the ccp sublattice structure for $x \geq 0.5$ samples rather than the pristine hcp sublattice structure. The In L_3-edge XANES spectra are associated with the transition of the In $2p_{3/2}$ state to unoccupied states above the Fermi level with In 5s and 5d characters, mostly 5s. Thus, the In L_3-edge XANES spectra is less asymmetric (Figure 2b) due to the spatial orientation of d orbitals.[22,23] There are mainly two differences in the spectra of the samples: the reduction of two shoulder peaks separated by 8 eV (at 3733 and 3741 eV) and a broadening peak at about ~3755 eV from $InCl_3$ to $Li_3Y_{0.8}In_{0.2}Cl_6$ with the lowest In content (inset in Figure 2b). For the Cl K-edge XANES spectra, all samples exhibit similar characteristic peaks at 2827 and 2829 eV (Figure 2). Moreover, another pre-edge feature at 2822.5 eV was observed, especially for the $Li_3Y_{1-x}In_xCl_6$ SSEs with high In^{3+} content, which is due to the covalent In metal-Cl ligand orbital mixing (Cl 3p orbitals and In 5d orbitals).[24] Clear and gradual changes of the main peak intensity of Y L_3-edges, In L_3-edges (insert in Figure 2a,b), and pre-edge of Cl K-edge can be seen. Qualitatively, for the Y L_3-edge, x = 0.2 is certainly more like Li_3YCl_6; for the Cl K-edge, the character associated with Li_3YCl_6 disappears when x is large, and the Cl K-edge becomes more similar to $InCl_3$.The same trend is also reflected from the evolution of the In L_3-edge. All these

https://dx.doi.org/10.1021/acs.nanolett.0c01156
Nano Lett. 2020, 20, 4384−4392

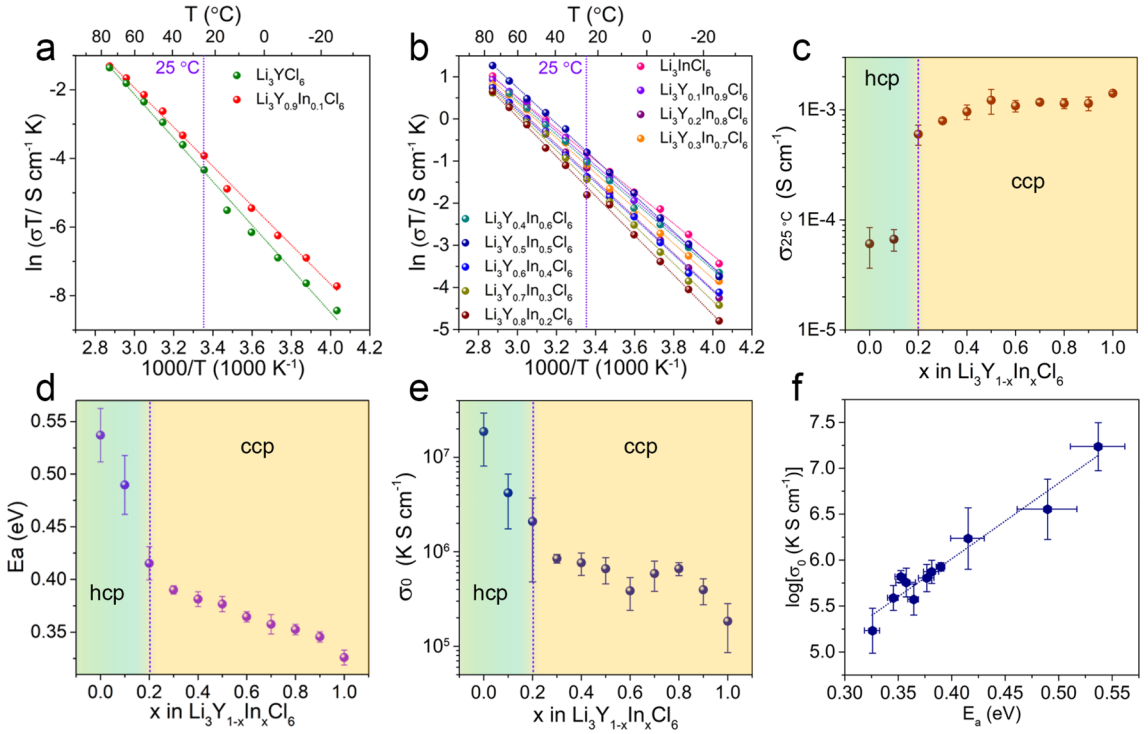

Figure 3. (a) Arrhenius plots of $Li_3Y_{1-x}In_xCl_6$ (x = 0, 0.1) and (b) $Li_3Y_{1-x}In_xCl_6$ (x = 0.2−1) obtained via temperature-dependent impedance plots. (c) Conductivity at 25 °C, (d) activation energy, and (e) Arrhenius prefactor σ_0 of $Li_3Y_{1-x}In_xCl_6$ ($0 \le x \le 1$). (f) Log of pre-exponential factor σ_0 in $\sigma = \sigma_0 \exp(-E_a/k_bT)/T$ vs activation energy E_a for $Li_3Y_{1-x}In_xCl_6$ ($0 \le x \le 1$). Error bars were figured with the standard deviation of 2−3 samples for each composition.

changes are consistent and should be correlated to the Y^{3+} and In^{3+} concentration change within the structure.

Y K-edge XAFS analysis was performed to reveal the local environment of Y in $Li_3Y_{1-x}In_xCl_6$ with a monoclinic structure (Figure 2d−i). The experimental EXAFS results of $Li_3Y_{1-x}In_xCl_6$ (x = 0.2, 0.4, 0.6, and 0.8) were compared in Figure 2d, with four features "a" to "d" observed and those of $Li_3Y_{1-x}In_xCl_6$ (x = 0.4, 0.6, and 0.8) are quite similar (insets of Figure 2d). Figure 2e shows the experimental EXAFS result of $Li_3Y_{0.2}In_{0.8}Cl_6$, demonstrating the nearest neighbor Y local environment. Two features of "A" and "B" in the R space were resolved by the first and second magnitude of Fourier transform (FT) EXAFS peaks (insets of Figure 2e). A further R space curve fitting was guided by the DFT modeled Y local environment with Feff theoretical scattering amplitudes and phases calculation.[25] The XAFS data and the R space fitting were performed by ATHENA software[26] and WINXAS,[27] respectively. The Feff R space fitting result shows good agreement with the experimental data as presented in Figure 2f in both the magnitude and imaginary part of the FT. Such good consistency is further reflected in the k space for $k^3\chi(k)$ between the experimental and the Feff modeling (Figure 2g) as well as the quite similar Y−Cl bond distance obtained by DFT and EXAFS (Table S5).

The Y local environment throughout experimentally resolved XANES features "a" to "d" (red line, Figure 2h) was verified by XANES theoretical modeling, which was performed in two cycles and guided by the DFT model and EXAFS result obtained through the R space curve fitting (Table S5).[28] The first cycle of XANES modeling (M-1 modeling) was performed over the Y centered spherical cluster developed from DFT prediction. The second cycle of XANES modeling (M-2 modeling) was performed by extending the M-1 modeling with the modified nearest neighbor bonding Y−Cl, Y−Li, and Y−In based on the R space curve fitting result (Table S5). The two modeling results presented in Figure 2h indicate that experimentally resolved XANES features "a" to "b" have all been reproduced by M-1 and M-2, and the modeling quality for "b" and "c" has been further improved by M-2 modeling (Figure 2i). Overall, the experimental XAFS features addressed by the EXAFS R space curve fitting and XANES theoretical modeling clearly support the local environment of Y in the In_1 site.

Li^+ ionic conductivities were measured with cold-pressed pellets at different temperatures. The variation of $Li_3Y_{1-x}In_xCl_6$ SSEs at 25 °C as a function of x in $Li_3Y_{1-x}In_xCl_6$ SSEs is displayed in Figures S3 and S4. Figure 3a,b shows Arrhenius plots of the $Li_3Y_{1-x}In_xCl_6$ SSEs. The activation energies (E_a) and Arrhenius prefactors (σ_0) were calculated using the equation

$$\sigma = \sigma_0 \exp(-E_a/k_BT)/T \quad (1)$$

where σ is ionic conductivity, T is the absolute temperature, and k_B is the Boltzmann constant.[29,30] The corresponding parameters of ionic conductivity (25 °C), E_a, and σ_0 of the $Li_3Y_{1-x}In_xCl_6$ SSEs are shown in Figure 3c−e, respectively. The ionic conductivity of the Li_3YCl_6 (orthorhombic) is ~6.08 × 10^{-5} S cm^{-1}. With the increase of In^{3+} substitution, the ionic conductivity of $Li_3Y_{0.9}In_{0.1}Cl_6$ SSEs with trigonal structure increased to 6.68 × 10^{-5} S cm^{-1} (Figure 3a,c). However, once the ccp anion structure appeared, the ionic conductivities are highly improved to 6.02 × 10^{-4} S cm^{-1} for $Li_3Y_{0.8}In_{0.2}Cl_6$ (Figure 3c), and all samples with $x \ge 0.5$ retained high ionic conductivity in the range from 1.09 to 1.42 × 10^{-3} S cm^{-1}. It is known that the ionic conductivity of SSE is highly dependent

https://dx.doi.org/10.1021/acs.nanolett.0c01156
Nano Lett. 2020, 20, 4384−4392

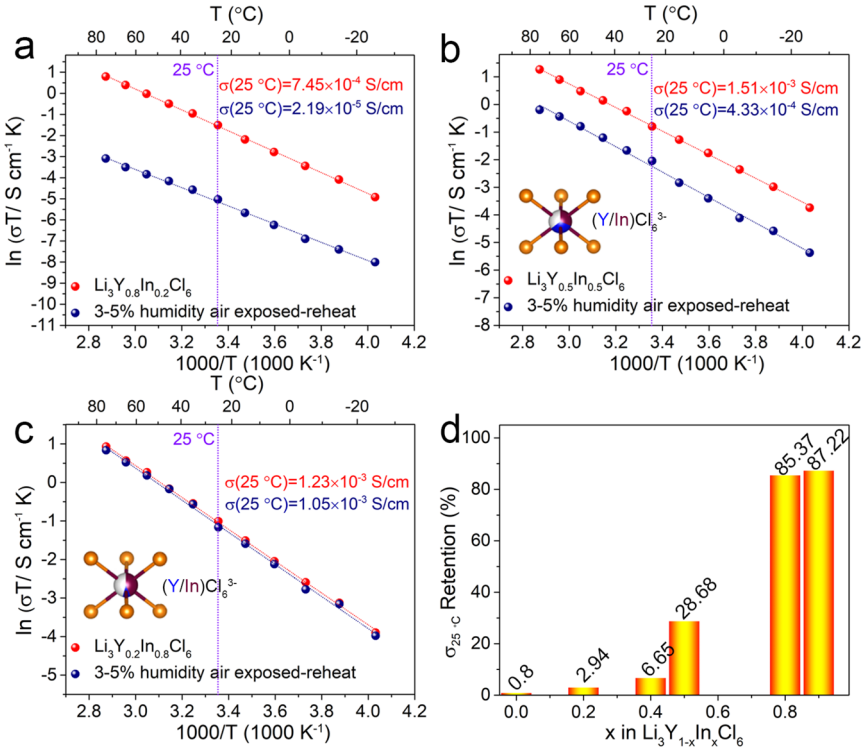

Figure 4. Comparison of the ionic conductivities of pristine $Li_3Y_{1-x}In_xCl_6$ SSEs (red) and $Li_3Y_{1-x}In_xCl_6$ SSEs after exposure to air with 3−5% humidity (blue) for 12 h and reheated at 260 °C for 1 h under a vacuum. Representative Arrhenius plots of (a) $Li_3Y_{0.8}In_{0.2}Cl_6$, (b) $Li_3Y_{0.5}In_{0.5}Cl_6$, and (c) $Li_3Y_{0.2}In_{0.8}Cl_6$ before and after air exposure, (d) Comparison of the ionic conductivity retention of $Li_3Y_{1-x}In_xCl_6$ SSEs before and after air exposure. The structures of $(Y/In)Cl_6^{3-}$ of $Li_3Y_{1-x}In_xCl_6$ ($x > 0.2$) SSEs with ccp sublattice are highlighted in the insets b and c.

on the structure, and most of the reported halide SSEs with high RT ionic conductivity over 10^{-3} S cm^{-1} possess ccp structure (such as Li_3YBr_6,[6] Li_3InCl_6,[7,8] Li_3ScCl_6,[10] and high-temperature phase Li_3InBr_6[31]). Thus, it can be inferred that the initial increase of ionic conductivity with In^{3+} substitution is mainly due to the induced structural change from pristine hcp to ccp anion sublattice. Another noticeable feature is that the ionic conductivities show no obvious change when $x \geq 0.5$, and the volume parameters of the unit cells shrink with the increase of In^{3+} content. This phenomenon is quite different from the previous opinion that ionic conductivity traditionally increases along with the increase in the unit cell volume or reaching an "optimal" size.[32,33] The ionic conductivity evolution of $Li_3Y_{1-x}In_xCl_6$ ($0 \leq x \leq 1$) indicates that the sublattice structure has a greater influence on the Li^+ conductivity. On the other hand, the E_a value of $Li_3Y_{1-x}In_xCl_6$ ($x = 0, 0.1$) SSEs with the hcp anion structure is much higher than the $Li_3Y_{1-x}In_xCl_6$ ($x \geq 0.3$) SSEs with the ccp anion structure, indicating a larger migration barrier for hcp than the ccp anion structure. Furthermore, the E_a value of $Li_3Y_{1-x}In_xCl_6$ ($x \geq 0.3$) SSEs gradually decreases along with the increase of In^{3+} content as shown in Figure 3d. It can be concluded that the sublattice structure influence is the more dominant factor for the E_a of $Li_3Y_{1-x}In_xCl_6$ SSEs. The detailed value of the fitting parameters, ionic conductivities, E_a, and σ_0 of $Li_3Y_{1-x}In_xCl_6$ SSEs are listed in Tables S6−S9.

The ionic conductivities of $Li_3Y_{1-x}In_xCl_6$ SSEs do not grow linearly with the decrease of E_a. That is reasonable because the σ_0 of $Li_3Y_{1-x}In_xCl_6$ SSEs changes significantly with In^{3+} content, as shown in Figure 3e, which is also consistent with other crystalline SSEs[29,34] with tuned components. Nevertheless, the phenomenon is quite different from the unchanged σ_0 for vitreous electrolytes.[35,36] It is believed that several factors act as key parameters dominating the ionic conductivities of SSEs including the concentration of mobile ions, the activation energy, and the activation entropy.[37] Among them, activation entropy, arising from the multiplicity of microstates during the ionic hopping process, has a significant effect on ionic conductivity. Correspondingly, the σ_o and the E_a for solid electrolytes are linked by the Meyer−Neldel rule (MNR)

$$\log \sigma_0 = aE_a + b \tag{2}$$

where a and b are the constants.[37,38] Related data were extracted from linear Arrhenius plots (Figure 3f). The linear relationship shows that the Meyer−Neldel rule is satisfied in all $Li_3Y_{1-x}In_xCl_6$ samples. When the In content in the SSEs is over 30%, both the σ_0 and E_a are significantly decreased, and thus, the ionic conductivity does not show much improvement even with the activation barrier reduced (Figure 3c,d). The variation of both along with the different amounts of In^{3+} content should be caused by the changed sublattice structure and unit cell parameters of the $Li_3Y_{1-x}In_xCl_6$ SSEs, while it seems the sublattice structure plays a predominant role.

The storage and fabrication conditions of SSEs are highly dependent on their humidity stability. However, most of the SSEs have been degraded when exposed to ambient air.[39−41] Li_3YCl_6 is not stable, even in low humidity, and will change to $YCl_3{\cdot}6H_2O$ and $LiCl{\cdot}H_2O$ after exposure air with 3−5% humidity for 12 h (Figure S5). Moreover, Li_3YCl_6 can not be recovered by reheating the "spoiled" sample in an inert atmosphere (Figures S6 and 7). Therefore, the ionic conductivities of pristine $Li_3Y_{1-x}In_xCl_6$ SSEs and reheated samples after humidity exposure were compared in Figure 4

https://dx.doi.org/10.1021/acs.nanolett.0c01156
Nano Lett. 2020, 20, 4384−4392

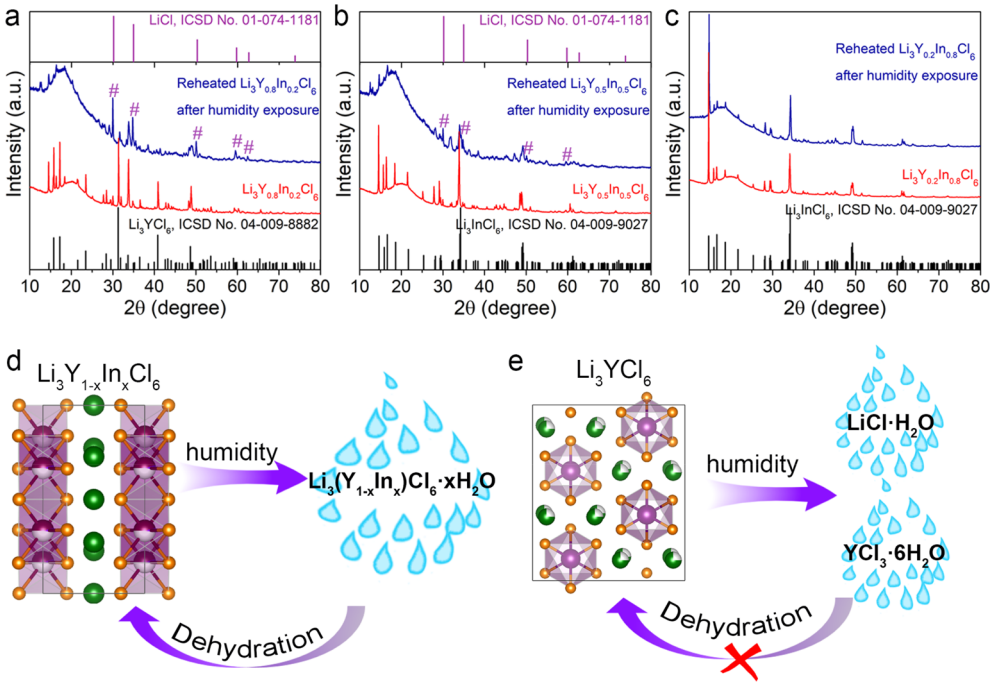

Figure 5. Comparison of the XRD patterns of pristine $Li_3Y_{1-x}In_xCl_6$ SSEs (red) and $Li_3Y_{1-x}In_xCl_6$ SSEs after exposure to air with 3−5% humidity (blue) for 12 h and reheated at 260 °C for 1 h under a vacuum. (a) $Li_3Y_{0.8}In_{0.2}Cl_6$, (b) $Li_3Y_{0.5}In_{0.5}Cl_6$, and (c) $Li_3Y_{0.2}In_{0.8}Cl_6$. Schematic illustration of the humidity stabilities of (d) $Li_3Y_{1-x}In_xCl_6$ and (e) Li_3YCl_6.

and Figures S8−10. The pristine $Li_3Y_{1-x}In_xCl_6$ (x = 0, 0.2, 0.4, 0.5, 0.8, and 0.9) SSEs exhibit RT ionic conductivities of 7.58×10^{-5}, 7.45×10^{-4}, 1.12×10^{-3}, 1.51×10^{-3}, 1.23×10^{-3}, and 1.26×10^{-3} S cm^{-1}, respectively; the reheated SSEs after humidity exposure show RT ionic conductivities of 6.06×10^{-7}, 2.19×10^{-5}, 7.45×10^{-5}, 4.33×10^{-4}, 1.05×10^{-3}, and 1.10×10^{-3} S cm^{-1}. The corresponded conductivity retention is 0.8%, 2.94%, 6.65%, 28.68%, 85.37%, and 87.22%, respectively. Obviously, when $x > 0.5$ in the $Li_3Y_{1-x}In_xCl_6$ SSEs, the conductivity retention after humidity exposure is significantly improved.

The structure evolution of $Li_3Y_{1-x}In_xCl_6$ SSEs after humidity exposure was first studied by Raman (Figure S11). Two obvious modes at 248 and 268 cm^{-1} for the Li_3YCl_6 sample after humidity exposure are due to the Y^{3+}-H_2O−Cl^- and Y^{3+}-Cl^- vibrations, which is similar to that of YCl_3 dissolved in the water.[42] The Raman spectra are totally different when enough In^{3+} was introduced, and an obvious mode at 282 cm^{-1} was detected. Such mode is similar to the reported hydrated indium compound intermediates such as $K_3InCl_6{\cdot}H_2O$[43] and $K_2InCl_5{\cdot}H_2O$,[44] indicating the possible formation of hydrated $Li_3Y_{1-x}In_xCl_6$ intermediates. This is further proved by the lack of the XRD signals of LiCl, $LiCl{\cdot}H_2O$, and $YCl_3{\cdot}6H_2O$ in the synchrotron-based XRD patterns of $Li_3Y_{0.2}In_{0.8}Cl_6$ after humidity exposure (Figure S12a), with some new XRD peaks (marked as *) appearing instead, which should be the hydrated $Li_3Y_{1-x}In_xCl_6$ intermediates. In contrast, the humidity exposed $Li_3Y_{1-x}In_xCl_6$ samples (x = 0.5, 0.6) with low In^{3+} content show obvious XRD signals of LiCl and $YCl_3{\cdot}6H_2O$ (Figure S12b). Thus, it can be concluded that, after humidity exposure, $Li_3Y_{1-x}In_xCl_6.xH_2O$ intermediates formed for $Li_3Y_{1-x}In_xCl_6$ samples with high In^{3+} content rather than separated $LiCl{\cdot}H_2O$ and $YCl_3{\cdot}6H_2O$ phases in the case of Li_3YCl_6.

The XRD results of the reheated $Li_3Y_{1-x}In_xCl_6$ SSEs after humidity exposure were further compared in Figure 5. Similar to Li_3YCl_6, obvious LiCl peaks have been observed when $x \leq 0.5$. Nevertheless, the XRD peaks of $Li_3Y_{1-x}In_xCl_6$ SSEs with $x > 0.5$ are almost the same as their pristine samples (Figure 5c, Figure S14). The stable structure of $Li_3Y_{1-x}In_xCl_6$ SSEs with $x > 0.5$ is believed to be due to the higher content of In.[7,8] The reversible conversion between Li_3InCl_6 and $Li_3InCl_6{\cdot}2H_2O$ and can be further proven by the existence of various kinds of hydrated indium halides, for example, $K_3InCl_6{\cdot}1.5H_2O$, $Rb_2InCl_5{\cdot}H_2O$, and $Cs_2InCl_5{\cdot}H_2O$.[45,46] Moreover, it is possible to obtain the anhydrous form from those hydrated indium halides.[8,47,48] Thus, as presented in Figure 5d, it is believed that, since both the incorporation of Y^{3+} and In^{3+} in $(Y/In)Cl_6^{3-}$ octahedra in the $Li_3Y_{1-x}In_xCl_6$ SSEs, when the In^{3+} content is high enough, the $(Y/In)Cl_6^{3-}$ octahedral structures may be retained after humidity exposure to form hydrated intermediates. Afterward, the $Li_3Y_{1-x}In_xCl_6$ SSEs can be reobtained after a careful dehydration process, which can guarantee a relatively high tolerance of $Li_3Y_{1-x}In_xCl_6$ SSEs toward humidity. In contrast, as aforementioned, the separated $LiCl{\cdot}H_2O$ and $YCl_3{\cdot}6H_2O$ phases obtained for humidity-exposed Li_3YCl_6 can not be converted back (Figure 5e).

The good humidity tolerance of $Li_3Y_{1-x}In_xCl_6$ SSEs was also reflected by XANES data of the Y L_3-edge, In L_3-edge, and Cl K-edge collected for the pristine and reheated samples (Figure S15). In addition to the conductivity and structure evolutions of $Li_3Y_{1-x}In_xCl_6$ SSEs, the morphologies of those SSEs before and after humidity exposure are also compared as shown in Figure S16. The scanning electron microscopy (SEM) images presented in Figure S16 indicate that $Li_3Y_{1-x}In_xCl_6$ SSEs with low In^{3+} content changed significantly (from the pristine small particles to numerous nanorods after humidity exposure). Nanorod-type morphology was reduced along with the increase of In^{3+} in $Li_3Y_{1-x}In_xCl_6$ SSEs. It should be noted

https://dx.doi.org/10.1021/acs.nanolett.0c01156
Nano Lett. 2020, 20, 4384−4392

that, although the structure of the $Li_3Y_{0.2}In_{0.8}Cl_6$ sample does not change significantly, as reflected by the XRD and XANES results, there is still obvious morphology change with some newly formed nanorods compared to its pristine small particles, which might be influenced by the dehydration process.

In conclusion, $Li_3Y_{1-x}In_xCl_6$ ($0 \le x \le 1$) was synthesized and the effect on the structural changes, ionic conductivity, as well as the influence of humidity tolerance was explored. The structure of $Li_3Y_{1-x}In_xCl_6$ gradually changes from the pristine hcp to a ccp anion arrangement along with an increase in In^{3+} content. Thus, the lithium substructure and the metal-Cl covalency are significantly changed. Once the ccp sublattice formed for $Li_3Y_{1-x}In_xCl_6$, the ionic conductivities can be improved to 10^{-3} S cm^{-1} at 25 °C, indicating that the sublattice evolution plays a key role in promoting fast Li^+ transport. Moreover, the humidity tolerance was highly improved when introducing In^{3+} into the $Li_3Y_{1-x}In_xCl_6$ SSEs. This work highlights the importance of the structural environment on the optimization of ionic conductivity and humidity tolerance in $Li_3Y_{1-x}In_xCl_6$ SSEs and further emphasizes that a better understanding of substructure effects on ionic transport and chemical stability is important.

■ ASSOCIATED CONTENT

Supporting Information

The Supporting Information is available free of charge at https://pubs.acs.org/doi/10.1021/acs.nanolett.0c01156.

Experimental procedures, the Rietveld refinement results, impedance plots, XRD patterns, comparison of the ionic conductivities, Raman spectra, Li^+ probability density, SEM images, atomic coordinates, occupation factor and isotropic displacement parameters, DFT model, capacitance (C) of the parallel combination CPE/R and impedance data fitting, ionic conductivities, the activation energy for all samples, and corresponding average and standard deviation for those samples, and the pre-exponential factor for all samples and corresponding average and standard deviation for those samples (PDF)

■ AUTHOR INFORMATION

Corresponding Authors

Ning Chen − *Canadian Light Source, Saskatoon, Saskatchewan S7N 2V3, Canada;* orcid.org/0000-0002-1269-6119; Email: ning.chen@lightsource.ca

Xueliang Sun − *Department of Mechanical and Materials Engineering, University of Western Ontario, London, Ontario N6A 3K7, Canada;* orcid.org/0000-0003-0374-1245; Email: xsun9@uwo.ca

Authors

Xiaona Li − *Department of Mechanical and Materials Engineering, University of Western Ontario, London, Ontario N6A 3K7, Canada*

Jianwen Liang − *Department of Mechanical and Materials Engineering, University of Western Ontario, London, Ontario N6A 3K7, Canada*

Keegan R. Adair − *Department of Mechanical and Materials Engineering, University of Western Ontario, London, Ontario N6A 3K7, Canada*

Junjie Li − *Department of Mechanical and Materials Engineering, University of Western Ontario, London, Ontario N6A 3K7, Canada*

Weihan Li − *Department of Mechanical and Materials Engineering, University of Western Ontario, London, Ontario N6A 3K7, Canada*

Feipeng Zhao − *Department of Mechanical and Materials Engineering, University of Western Ontario, London, Ontario N6A 3K7, Canada*

Yongfeng Hu − *Canadian Light Source, Saskatoon, Saskatchewan S7N 2V3, Canada*

Tsun-Kong Sham − *Department of Chemistry, University of Western Ontario, London, Ontario N6A 3K7, Canada;* orcid.org/0000-0003-1928-6697

Li Zhang − *China Automotive Battery Research Institute Co. Ltd, Beijing 100088, China*

Shangqian Zhao − *China Automotive Battery Research Institute Co. Ltd, Beijing 100088, China*

Shigang Lu − *China Automotive Battery Research Institute Co. Ltd, Beijing 100088, China*

Huan Huang − *Glabat Solid-State Battery Inc., London, Ontario N6G 4X8, Canada*

Ruying Li − *Department of Mechanical and Materials Engineering, University of Western Ontario, London, Ontario N6A 3K7, Canada*

Complete contact information is available at: https://pubs.acs.org/10.1021/acs.nanolett.0c01156

Author Contributions

#Xiaona Li, Jianwen Liang, and Keegan R. Adair contributed equally to this work.

Notes

The authors declare no competing financial interest.

■ ACKNOWLEDGMENTS

This research was supported by the Natural Sciences and Engineering Research Council of Canada (NSERC), GLABAT Solid-State Battery Inc., Canada Research Chair Program (CRC), Canada Foundation for Innovation (CFI), Ontario Research Fund, the Canada Light Source at University of Saskatchewan (CLS), Canada MITACS fellowships, and University of Western Ontario. We also appreciate the help of the beamline scientists of the Very Sensitive Elemental and Structural Probe Employing Radiation from a Synchrotron (VESPERS) beamline at CLS, Dr. Renfei Feng, and Dr. Peter Blanchard.

■ REFERENCES

(1) Famprikis, T.; Canepa, P.; Dawson, J. A.; Islam, M. S.; Masquelier, C. Fundamentals of inorganic solid-state electrolytes for batteries. *Nat. Mater.* **2019**, *18*, 1278−1291.

(2) Chen, R.; Li, Q.; Yu, X.; Chen, L.; Li, H. Approaching Practically Accessible Solid-State Batteries: Stability Issues Related to Solid Electrolytes and Interfaces. *Chem. Rev.* **2019**.

(3) Zhao, Q.; Stalin, S.; Zhao, C.-Z.; Archer, L. A. Designing solid-state electrolytes for safe, energy-dense batteries. *Nat. Rev. Mater.* **2020**, *5*, 229−252.

(4) Wang, S.; Bai, Q.; Nolan, A. M.; Liu, Y.; Gong, S.; Sun, Q.; Mo, Y. Lithium Chlorides and Bromides as Promising Solid-State Chemistries for Fast Ion Conductors with Good Electrochemical Stability. *Angew. Chem., Int. Ed.* **2019**, *58*, 8039−8043.

(5) Li, X.; Liang, J.; Yang, X.; Adair, K. R.; Wang, C.; Zhao, F.; Sun, X. Progress and Perspectives of Halide-based Lithium Conductors for All-Solid-State Batteries. *Energy Environ. Sci.* **2020**.
(6) Asano, T.; Sakai, A.; Ouchi, S.; Sakaida, M.; Miyazaki, A.; Hasegawa, S. Solid Halide Electrolytes with High Lithium-Ion Conductivity for Application in 4 V Class Bulk-Type All-Solid-State Batteries. *Adv. Mater.* **2018**, *30*, 1803075.
(7) Li, X.; Liang, J.; Luo, J.; Norouzi Banis, M.; Wang, C.; Li, W.; Deng, S.; Yu, C.; Zhao, F.; Hu, Y.; Sham, T.-K.; Zhang, L.; Zhao, S.; Lu, S.; Huang, H.; Li, R.; Adair, K. R.; Sun, X. Air-stable Li_3InCl_6 electrolyte with high voltage compatibility for all-solid-state batteries. *Energy Environ. Sci.* **2019**, *12*, 2665−2671.
(8) Li, X.; Liang, J.; Chen, N.; Luo, J.; Adair, K. R.; Wang, C.; Banis, M. N.; Sham, T.-K.; Zhang, L.; Zhao, S.; Lu, S.; Huang, H.; Li, R.; Sun, X. Water-Mediated Synthesis of a Superionic Halide Solid Electrolyte. *Angew. Chem., Int. Ed.* **2019**, *58*, 16427−16432.
(9) Park, K.-H.; Kaup, K.; Assoud, A.; Zhang, Q.; Wu, X.; Nazar, L. F. High Voltage Superionic Halide Solid Electrolytes for All-Solid-State Li-Ion Batteries. *ACS Energy Letters* **2020**, *5*, 533−539.
(10) Liang, J.; Li, X.; Wang, S.; Adair, K. R.; Li, W.; Zhao, Y.; Wang, C.; Hu, Y.; Zhang, L.; Zhao, S.; Lu, S.; Huang, H.; Li, R.; Mo, Y.; Sun, X. Site-Occupation-Tuned Superionic Li_xScCl_{3+x} Halide Solid Electrolytes for All-Solid-State Batteries. *J. Am. Chem. Soc.* **2020**, *142*, 7012−7022.
(11) Weppner, W.; Huggins, R. Ionic conductivity of solid and liquid $LiAlCl_4$. *J. Electrochem. Soc.* **1977**, *124*, 35−38.
(12) Kanno, R.; Takeda, Y.; Takada, K.; Yamamoto, O. Ionic Conductivity and Phase Transition of the Spinel System $Li_{2-2x}M_{1+x}Cl_4$ (M= Mg, Mn, Cd). *J. Electrochem. Soc.* **1984**, *131*, 469−474.
(13) Kanno, R.; Takeda, Y.; Takada, K.; Yamamoto, O. Phase diagram and ionic conductivity of the lithium chloride-iron (II) chloride system. *Solid State Ionics* **1983**, *9*, 153−156.
(14) Schlem, R.; Muy, S.; Prinz, N.; Banik, A.; Shao-Horn, Y.; Zobel, M.; Zeier, W. G. Mechanochemical Synthesis: A Tool to Tune Cation Site Disorder and Ionic Transport Properties of Li_3MCl_6 (M = Y, Er) Superionic Conductors. *Adv. Energy Mater.* **2020**, *10*, 1903719.
(15) Muy, S.; Voss, J.; Schlem, R.; Koerver, R.; Sedlmaier, S. J.; Maglia, F.; Lamp, P.; Zeier, W. G.; Shao-Horn, Y. High-throughput screening of solid-state Li-ion conductors using lattice-dynamics descriptors. *iScience* **2019**, *16*, 270−282.
(16) Bohnsack, A.; Stenzel, F.; Zajonc, A.; Balzer, G.; Wickleder, M. S.; Meyer, G. Ternäre Halogenide vom Typ A_3MX_6. VI [1]. Ternäre Chloride der Selten-Erd-Elemente mit Lithium, Li_3MCl_6 (M = Tb·Lu, Y, Sc): Synthese, Kristallstrukturen und Ionenbewegung. *Z. Anorg. Allg. Chem.* **1997**, *623*, 1067−1073.
(17) Schmidt, M. O.; Wickleder, M. S.; Meyer, G. Zur Kristallstruktur von Li_3InCl_6. *Z. Anorg. Allg. Chem.* **1999**, *625* (4), 539−540.
(18) Steiner, H.-J.; Lutz, H. D. Neue schnelle Ionenleiter vom Typ $M_3^IM^{III}Cl_6$ (M^I = Li, Na, Ag; M^{III} = In, Y). *Z. Anorg. Allg. Chem.* **1992**, *613*, 26−30.
(19) Shannon, R. D. Revised effective ionic radii and systematic studies of interatomic distances in halides and chalcogenides. *Acta Crystallogr., Sect. A: Cryst. Phys., Diffr., Theor. Gen. Crystallogr.* **1976**, *32*, 751−767.
(20) Rogalev, A.; Goulon, J.; Wilhelm, F.; Brouder, C.; Yaresko, A.; Ben Youssef, J.; Indenbom, M.V. Element selective X-ray magnetic circular and linear dichroisms in ferrimagnetic yttrium iron garnet films. *J. Magn. Magn. Mater.* **2009**, *321*, 3945−3962.
(21) Blanchard, P. E.; Liu, S.; Kennedy, B. J.; Ling, C. D.; Zhang, Z.; Avdeev, M.; Cowie, B. C.; Thomsen, L.; Jang, L.-Y. Investigating the order−disorder phase transition in $Nd_{2-x}Y_xZr_2O_7$ via diffraction and spectroscopy. *Dalton Trans* **2013**, *42*, 14875−14882.
(22) Figueiredo, M.-O.; Silva, T.; Oliveira, D.; Rosa, D. Indium-carrier minerals in polymetallic sulphide ore deposits: a crystal chemical insight into an indium binding state supported by X-ray absorption spectroscopy data. *Minerals* **2012**, *2*, 426−434.
(23) Demchenko, I. N.; Chernyshova, M.; Piskorska-Hommel, E.; Minikayev, R.; Domagala, J.; Yamaguchi, T.; Stolte, W. C.; Lawniczak-Jablonska, K. An XANES and XES investigation of the electronic structure of indium rich $In_xGa_{1-x}N$ films. *J. Alloys Compd.* **2011**, *509*, 9528−9535.
(24) Loble, M. W.; Keith, J. M.; Altman, A. B.; Stieber, S. C. E.; Batista, E. R.; Boland, K. S.; Conradson, S. D.; Clark, D. L.; Lezama Pacheco, J.; Kozimor, S. A.; Martin, R. L.; Minasian, S. G.; Olson, A. C.; Scott, B. L.; Shuh, D. K.; Tyliszczak, T.; Wilkerson, M. P.; Zehnder, R. A. Covalency in Lanthanides. An X-ray Absorption Spectroscopy and Density Functional Theory Study of $LnCl_6^{x-}$(x= 3, 2). *J. Am. Chem. Soc.* **2015**, *137*, 2506−2523.
(25) Rehr, J. J.; Albers, R. C. Theoretical approaches to x-ray absorption fine structure. *Rev. Mod. Phys.* **2000**, *72*, 621.
(26) Ravel, B.; Newville, M. ATHENA, ARTEMIS, HEPHAESTUS: data analysis for X-ray absorption spectroscopy using IFEFFIT. *J. Synchrotron Radiat.* **2005**, *12*, 537−541.
(27) Ressler, T. WinXAS: A new software package not only for the analysis of energy-dispersive XAS data. *J. Phys. IV* **1997**, *7*, C2-269−C2-270.
(28) Joly, Y. X-ray absorption near-edge structure calculations beyond the muffin-tin approximation. *Phys. Rev. B: Condens. Matter Mater. Phys.* **2001**, *63*, 125120.
(29) Krauskopf, T.; Pompe, C.; Kraft, M. A.; Zeier, W. G. Influence of Lattice Dynamics on Na+ Transport in the Solid Electrolyte $Na_3PS_{4-x}Se_x$. *Chem. Mater.* **2017**, *29*, 8859−8869.
(30) Bernges, T.; Culver, S. P.; Minafra, N.; Koerver, R.; Zeier, W. G. Competing Structural Influences in the Li Superionic Conducting Argyrodites $Li_6PS_{5-x}Se_xBr$ ($0 \leq x \leq 1$) upon Se Substitution. *Inorg. Chem.* **2018**, *57*, 13920−13928.
(31) Yamada, K.; Iwaki, K.; Okuda, T.; Tomita, Y. Impedance Spectroscopy and Structural Investigation of Li^+ Conductor Li_3InBr_6. In *Solid State Ionics: Trends in the New Millennium*; World Scientific, 2002; pp 621−628.
(32) Zhang, L.; Yang, K.; Mi, J.; Lu, L.; Zhao, L.; Wang, L.; Li, Y.; Zeng, H. Na_3PSe_4: A novel chalcogenide solid electrolyte with high ionic conductivity. *Adv. Energy Mater.* **2015**, *5*, 1501294.
(33) Wang, N.; Yang, K.; Zhang, L.; Yan, X.; Wang, L.; Xu, B. Improvement in ion transport in Na_3PSe_4−Na_3SbSe_4 by Sb substitution. *J. Mater. Sci.* **2018**, *53*, 1987−1994.
(34) Muy, S.; Bachman, J. C.; Chang, H.-H.; Giordano, L.; Maglia, F.; Lupart, S.; Lamp, P.; Zeier, W. G.; Shao-Horn, Y. Lithium Conductivity and Meyer−NeldelRule in Li_3PO_4−Li_3VO_4−Li_4GeO_4 Lithium Superionic Conductors. *Chem. Mater.* **2018**, *30*, 5573−5582.
(35) Petrowsky, M.; Frech, R. Temperature dependence of ion transport: the compensated Arrhenius equation. *J. Phys. Chem. B* **2009**, *113*, 5996−6000.
(36) Souquet, J. Ionic transport in glassy electrolytes. In *Solid State Electrochemistry*; Cambridge University: Cambridge, 1995; pp 74−79.
(37) Almond, D.; West, A. The activation entropy for transport in ionic conductors. *Solid State Ionics* **1987**, *23*, 27−35.
(38) Dosdale, T.; Brook, R. Cationic conduction and diffusion and the compensation law. *J. Mater. Sci.* **1978**, *13*, 167−172.
(39) Liu, X.; Chen, Y.; Hood, Z. D.; Ma, C.; Yu, S.; Sharafi, A.; Wang, H.; An, K.; Sakamoto, J.; Siegel, D. J.; Cheng, Y.; Jalarvo, N. H.; Chi, M. Elucidating the mobility of H^+ and Li^+ ions in ($Li_{6.25-x}H_xAl_{0.25}$) $La_3Zr_2O_{12}$ via correlative neutron and electron spectroscopy. *Energy Environ. Sci.* **2019**, *12*, 945−951.
(40) Brugge, R. H.; Hekselman, A. O.; Cavallaro, A.; Pesci, F. M.; Chater, R. J.; Kilner, J. A.; Aguadero, A. Garnet electrolytes for solid state batteries: visualization of moisture-induced chemical degradation and revealing its impact on the Li-ion dynamics. *Chem. Mater.* **2018**, *30*, 3704−3713.
(41) Hayashi, A.; Muramatsu, H.; Ohtomo, T.; Hama, S.; Tatsumisago, M. Improvement of chemical stability of Li_3PS_4 glass electrolytes by adding M_xO_y (M= Fe, Zn, and Bi) nanoparticles. *J. Mater. Chem. A* **2013**, *1*, 6320−6326.
(42) Rudolph, W. W.; Irmer, G. Hydration and ion pair formation in aqueous Y^{3+}−salt solutions. *Dalton Trans* **2015**, *44*, 18492−18505.
(43) Lorriaux-Rubbens, A.; Wallart, F.; Wignacourt, J.; Barbier, P.; Mairesse, G. Structural investigation of indium halide compounds:

https://dx.doi.org/10.1021/acs.nanolett.0c01156
Nano Lett. 2020, 20, 4384−4392

Single crystal Raman study of monohydrated potassium hexachloroindate. *Spectrochim. Acta Part A* **1981**, *37*, 1021−1027.
(44) Wignacourt, J.; Lorriaux-Rubbens, A.; Barbier, P.; Mairesse, G.; Wallart, F. Structural study of $K_2InCl_5 \cdot H_2O$ by X-Ray, Raman and IR spectroscopies. *Spectrochimica Acta Part A: Molecular Spectroscopy* **1980**, *36*, 403−411.
(45) Kartzmark, E. M. Double salts of indium trichloride with the alkali chlorides, with ammonium chloride, and with indium sulfate. *Can. J. Chem.* **1977**, *55*, 2792−2798.
(46) Kartzmark, E. M. The phase diagrams of the chlorides of the metals of Groups IIa and IIb with indium trichloride and water at 24° C. *Can. J. Chem.* **1980**, *58*, 539−545.
(47) Wignacourt, J.; Mairesse, G.; Abraham, F. Potassium tetrabromoindate (III), K $[InBr_4]$. *Acta Crystallogr., Sect. C: Cryst. Struct. Commun.* **1984**, *40*, 2006−2007.
(48) Atkinson, A.; Field, B. Complex indium-chlorine compounds obtained from solution. *J. Inorg. Nucl. Chem.* **1970**, *32*, 2601−2606.

https://dx.doi.org/10.1021/acs.nanolett.0c01156
Nano Lett. 2020, 20, 4384−4392